

Addressing single molecular spin with graphene based nano-architectures.

A.Candini¹, S. Lumetti^{1,2}, C. Godfrin³, F. Balestro^{3,4}, W. Wernsdorfer³, S. Klyatskaya⁵, M. Ruben^{5,6}, M. Affronte^{1,2}

¹ CNR, Institute Nanosciences, S3 Modena, via G. Campi 213A, 41124 Modena, Italy.

² Dipartimento di Scienze Fisiche, Informatiche, Matematiche, via G. Campi 213A, 41124 Modena, Italy.

³ Institut Néel-CNRS-UJF-INPG, UPR2940 25 rue des Martyrs BP 166, 38042 Grenoble cedex 9, France.

⁴ Institut Universitaire de France, 103 boulevard Saint-Michel, 75005 Paris, France.

⁵ Institute of Nanotechnology, Karlsruhe Institute of Technology (KIT), D-76344 Eggenstein-Leopoldshafen, Germany

⁶ Institut de Physique et Chimie des Matériaux de Strasbourg, UMR 7504 UdS-CNRS, 67034 Strasbourg Cedex 2, France

Abstract: *Finding reliable methods to exploit molecular degrees of freedom represents an intriguing problem involving the control of new mechanisms at the nano-scale and several technological challenges. Here we report a novel approach to address single molecular spin embedded in an electronic circuit. Our devices make use of molecules with well-defined magnetic anisotropy (TbPc₂) embedded in nano-gapped electrodes obtained by electro-burning graphene layers. Such devices work as molecular spin transistors allowing the detection of the Tb spin flip during the sweep of an external magnetic field. The spin read out is made by the molecular quantum dot that, in turns, is driven by an auxiliary gate voltage. In the general context of (spin-)electronics, these results demonstrate that: 1) molecular quantum dots can be used as ultra-sensitive detectors for spin flip detection and 2) the use of graphene electrodes as platform to contact organo-metallic molecule is a viable route to design more complex nano-architectures.*

Keywords: *molecular spin transistor, graphene based nano-junctions, molecular quantum dots.*

1. Introduction.

The giant leaps in performance from the first computing machines to today's mobile devices are due to a large extent to the miniaturization of their active components. Currently, further downscaling is becoming an enormous technological challenge, since the device sizes are reaching the ultimate limit of the atomic and molecular scale. Experimental findings in electron transport through single molecules put forth the idea that the use of single molecules in electronics could represent the next goal of miniaturization of electronic devices (Sun, 2014). Indeed, since the first proposal to use single molecules as an electronic component in 1974 (Aviram, 1974), much effort has been put into downscaling devices to the single-molecule level. Three terminal devices (transistors) constitute the reference elements for logic electronics and in 2000 the first single-molecule transistor was realized (Park H. P., 2000). In this molecular device the current between source and drain passed through a single C_{60} molecule, and it was regulated by the voltage applied on the gate electrode.

On the single molecule scale, the main advantage offered by the use of a gate electrode consists in the possibility to gain deeper insight into the electronic structure of the molecular system. By applying a voltage on the gate, it is indeed possible to change the electrostatic potential of the molecule, thereby inducing energy shifts of the molecular transport levels from which additional spectroscopic information about the molecule can be obtained, such as the presence of vibrational modes and excited states (Park H. P., 2000; Osorio, 2007). Gate electrodes can also be used to change the charge state of a molecule (i.e. oxidize or reduce it) (Kubatkin, 2003) and investigate higher-order transport processes such as cotunneling and the Kondo effect (Park J. P., 2002; Liang, 2002).

Despite the impressive progresses made in molecular electronics, addressing a single molecule still implies several technological challenges. The central one is certainly how to embed single molecules in electronic circuits in a reliable way suitable for mass production of devices (Lörtscher, 2013). Beside scanning probe techniques (Bumm, 1996), the most popular approaches to fabricate molecular junctions are mechanical break junctions (Reed, 1997) and electro-migrated junctions (Park H. L., 1999). Gold is the preferred material for realizing such molecular electrodes, since it is a noble metal and it is (relatively) easy to handle. The use of gold, however, has several drawbacks: the mobility of the atoms limits the stability of the junctions and their use for room temperature operations (Lörtscher, 2013; Moth-Poulsen, 2009; Ratner, 2013). Moreover, the proximity of metal electrodes may significantly perturb the molecular energy levels (Perrin, (2013)). Recently, the use of graphene as material for molecular-scale electrodes has been proposed as a valid alternative (Sun, 2014). With respect to metallic contacts, graphene offers a planar geometry with a thickness comparable to the molecular size. Moreover, the possibility to exploit molecular functionalizations to attach the molecular units to the graphene electrodes via carbon bonds and/or π stacking looks straightforward from a chemical point of view. Carbon-carbon

bonds are expected to lower the energy gap between the chemical potential of the electrodes and the LUMO/ HOMO molecular levels, thus decreasing the effective Schottky barrier at the molecular junction. Based on these considerations, several theoretical works have investigated the possibility to use graphene as an electrode to contact individual molecules (Bergvall, 2011; García-Suárez, 2013; Ryndyk, 2012; Péterfalvi, 2012; Prasongkit, 2013; Pshenichnyuk, 2013), predicting specific features such as quantum coherent transport (Bergvall, 2011), edge effects (Ryndyk, 2012), suppression of conductance fluctuations (Péterfalvi, 2012).

Recent pioneering works have demonstrated that it is possible to successfully use graphene for the realization of electrodes in molecular devices (Prins F. B.-A., 2011; Cao Y. D., 2012). More specifically, parallel multi-junctions devices have been fabricated in CVD graphene by using electron beam lithography and plasma etching (Cao Y. D., 2012; Jia, 2013; Cao Y. D., 2013). In order to address individual molecule, the electro-burning (EB) technique has been employed on exfoliated few-layer graphene on substrate, showing electrostatic molecular gating in molecular units at room temperature (Prins F. B.-A., 2011). It is worth noting that the yield of fabrication of nm-size gaps can be increased from about 50% (Burzurí E. P., 2012) to more than 95% by performing the EB process under vacuum on single layer graphene (Nef, 2014; Lau, 2014).

Based on these premises, the choice of the graphitic architecture for molecular (spin)electronics appears particularly appealing (Sun, 2014). In view of scalable platforms suitable for a mass production of molecular-scale devices, the use of large area graphene actually appears as one of the most appropriate choices. However, most of the methods suitable for the production of large area graphene, such as chemical vapor deposition (CVD) (Kim, 2009), are optimized to obtain continuous films of monolayer graphene, whose electrical properties are strongly affected by the application of a gate bias. The use of few-layer graphene, which is still thin but much less gate dependent than single layer (Prins F. B.-A., 2011; Burzurí E. P., 2012), seems therefore preferable for molecular electronics.

While many electronic features have been studied so far by molecular devices, it is clear that specific magnetic features of molecules may actually act as additional resource for logic circuits. In this framework, single-molecule magnets constitute a particularly interesting class of molecules, as their magnetic properties provide a unique fingerprint to recognize the presence of a single molecule within a nanojunction (Zyasin, 2010; Vincent, 2012; Burzurí E. Z., 2012). Of particular interest here are molecules with well-defined magnetic anisotropy that can be easily recognized and exploited even at single molecule level. A prototypical device is therefore the molecular spin-transistor proposed in Ref. (Bogani, 2008), made of a single-electron transistor (SET) with non-magnetic electrodes and a single magnetic molecule as the conducting island.

Here we report on the realization and functioning of three-terminal molecular devices in which a prototypical single-molecule magnet (TbPc_2) is embedded between two nanometer-spaced graphene-based electrodes. The bis(phthalocyanine) terbium(III) single ion magnet (TbPc_2 hereafter, see figure 7a) has been already used for the realization of molecular spin transistors with gold electrodes and it

was shown how it is possible to read out the electronic and the nuclear spin of an isolated Tb^{3+} ion (Vincent, 2012) as well as to coherently manipulate the nuclear spin (Thiele, 2014). For the electrodes, we chose to utilize graphene grown on the C-face of SiC (Forbeaux, 1998; Berger, 2004; Ohta, 2006; Virojanadara, 2008) since it can be grown on large areas and display a very small dependence on the external electric field. Molecular junctions are obtained by electroburning (see section 3) with a gate electrode laterally approaching the nanogap.

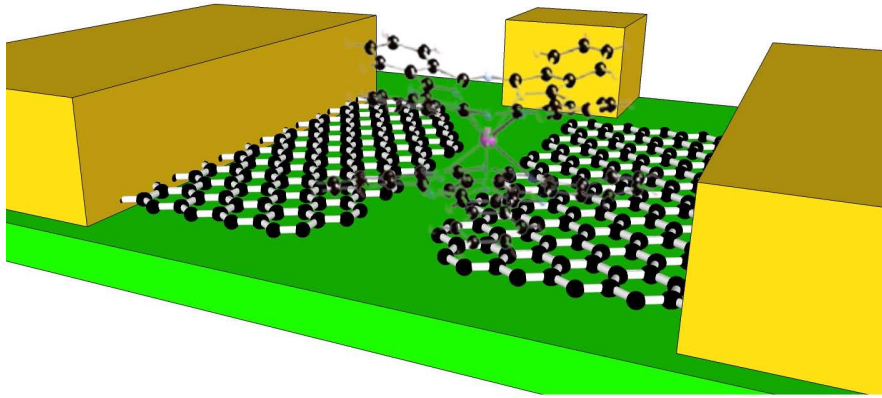


Figure 1 Artistic view of the hybrid molecular device with graphene electrodes and TbPc_2 magnetic molecule in the junction.

2 Molecular spin transistor.

The functioning of a molecular spin transistor is schematized in figure 2. The energy spectrum of molecules is characterized by discrete electronic energy levels: therefore, the charge transport through such a device can be described as a quantum dot in the junction (figure 2). The presence of the electrodes (which act as reservoirs for charge carriers) causes the molecular states to hybridize with the states of graphene: electrons can therefore tunnel from and to the molecule with finite probability. When the energy broadening of the levels due to hybridization is smaller than the charging energy U of the molecule, then the molecule is weakly coupled to the electrodes. This is the case expected in using graphene electrodes. At low temperatures, electron transport is blocked (figure 3a) except for gate voltages V_g bringing the molecular levels in resonance with the chemical potential of the electrodes (figure 3b) or for source-drain bias voltages aligning the chemical

potential of one of the electrodes with a molecular level (figure 3c). This transport regime, known as Coulomb blockade, gives rise to large regions of suppressed conductance, forming characteristic Coulomb diamonds in differential conductance plots (Hanson, 2007). Vibrational and spin excitation states can lead to resonance levels and appear inside the diamonds as well, which makes transport measurements essentially a form of spectroscopy.

For the TbPc_2 molecule, a molecular quantum dot is formed in the organic Pc ligands. It is worth to note that in the neutral derivative $[\text{TbPc}_2]^0$ used in our experiments there is an unpaired electron delocalized over the two Pc ligands as $S = 1/2$ radical and this probably facilitates the creation of the molecular quantum dot, although other features may well induce charge transport through other molecules with no radical. It has been shown that the anisotropic magnetic moment of the Tb^{3+} ion is coupled to the organic Pc_2 ligands by an indirect exchange interaction (Candini A. e., 2016). Consequently, the energy levels of the molecular quantum dot, through which the charge is flowing, are split by the coupling with the Tb spin moment. At low temperatures the Tb spin reversal is detected through jumps observed in the conductivity by sweeping the magnetic field.

Interestingly, these jumps are detected at very specific field values, corresponding to the allowed quantum tunneling resonances for the Tb electron spin, split by the hyperfine coupling with the nuclear moment (see par.4). This mechanism allows for an unambiguous identification of the molecule under investigation.

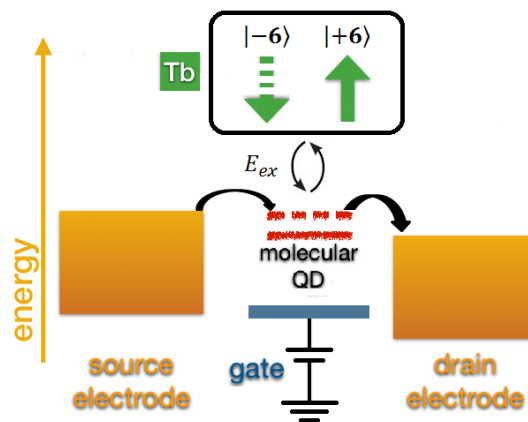


Figure 2. Scheme of a molecular spin transistor. The molecule behaves as a quantum dot with a discrete spectrum of energy levels (red lines) which can be tuned by the gate potential (blue) and aligned to the Fermi level of the electrodes (yellow). The spin state of the metal center (Tb in the case of TbPc_2) affects the energy levels of the quantum dot by effectively changing the conductivity of the device for any spin flip event.

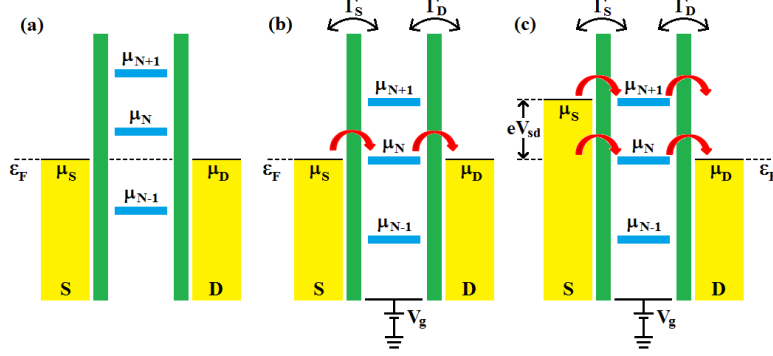


Figure 3. Transport through a molecular junction (μ_N , μ_{N-1} and μ_{N+1} denote the molecular levels, whereas μ_S and μ_D are the chemical potentials of source and drain electrodes, respectively). (a) Out of resonance, electrons cannot pass through the device. (b) Upon application of a gate voltage V_g , the molecular levels can be put in resonance with the chemical potentials of the electrodes and electrons can thus tunnel through the barrier. (c) By applying a bias voltage V_{sd} , the chemical potential of the electrodes is shifted and, as soon as it aligns with one or more molecular levels, the blockade is lifted and current flows (free elaboration from ref. (Bogani, 2008)).

3 Fabrication of graphene-based electrodes.

In the following we describe the procedure we are using to realize graphene based-electrodes. Turbostratic graphene is obtained on on-axis SiC(000-1) wafer. Firstly, the SiC substrate is hydrogen-etched in order to obtain atomically flat surfaces (Frewin, 2009), in a cold-wall reactor (high-temperature Aixtron BM) at temperature $T = 1350$ °C and pressure $P = 450$ mbar for 10 min. Afterwards, graphene is obtained in the same reactor through thermal decomposition of SiC (Starke, 2012) heating the wafer at $T = 1420$ °C for 90min in an argon atmosphere. Due to the higher vapor pressure of silicon with respect to carbon, the Si atoms evaporate leaving graphene layers behind. Attenuation of the SiC signal in Raman spectra is used to estimate the number of grown layers (Shivaraman, 2009), which are found to be about ten (Candini A. R., 2015). In addition, combined Raman and atomic force microscopy (AFM) analyses reveal a good homogeneity and quality of the resulting graphene (Starke, 2012; Candini A. R., 2015).

Electrical contacts are fabricated by electron beam lithography (EBL) through the following steps. Firstly, 3 nm Cr/30 nm Au are thermally deposited as the initial metal contacts in order to assure good ohmic contacts. Subsequently, graphene is patterned in the desired geometry by reactive ion etching (RIE) in an oxygen plasma. Finally, the connections from the initial metal contacts to the pads and the lateral gates are obtained by the evaporation of 5nm Cr/ 50nm Au.

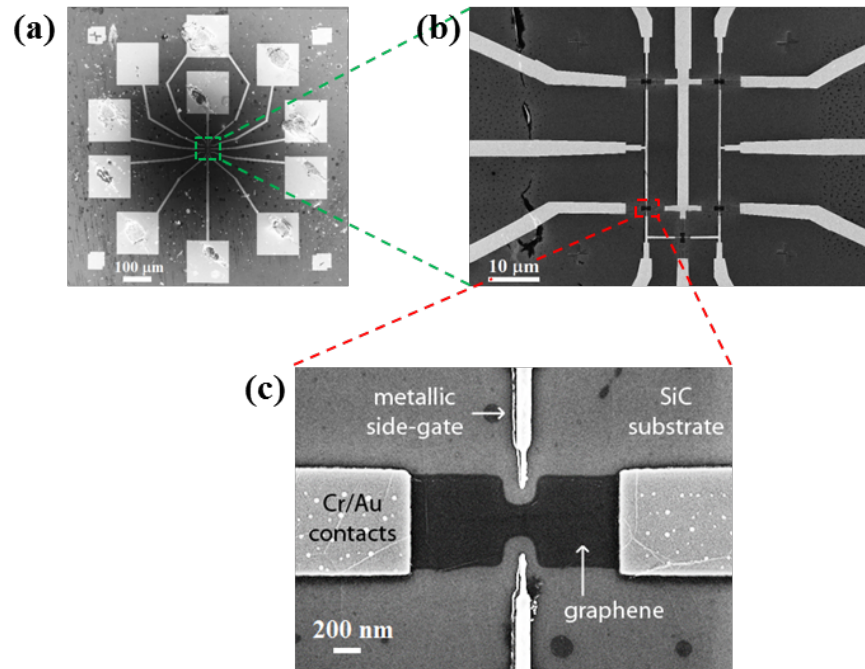


Figure 4. (a)-(b) SEM images showing the typical lineup of metal pads and electrodes and related graphene-based architecture (c) SEM image of a typical graphene device after fabrication: the middle “notched” graphene region is reduced to ~200 nm in width by plasma etching and the lateral gate electrodes are located at a distance of 50-100 nm.

Figures 4a and 4b show an overview of a typical pattern array, whereas the scanning electron microscope (SEM) image in figure 4c focuses on one of the graphene devices. The nanometer-sized gap in the graphene pads is finally opened via a feedback-controlled electroburning (EB) procedure (Prins F. B.-A., 2011), that can also be used for mechanically exfoliated flakes and chemically synthesized turbostratic graphene (Candini A. R., 2015). The EB process occurs thanks to the chemical reaction of carbon atoms with oxygen at high temperatures, induced by Joule heating at large current densities. The presence of a fast feedback loop (similar to what is employed for the electromigration of metallic nanowires (Thiele, 2014; Prins F. H., 2009)) is vital to avoid the abrupt breaking of the junction and it allows a precise control on the final structure of the molecular-sized junction.

We perform the feedback-controlled EB in air at room temperature: an increasing voltage (V) ramp (typically 0.1 V/s) is applied to the graphene junction, while the current (I) is continuously recorded so that the variations in the resistance ($R = V/I$) can be monitored. As soon as R increases by more than a predefined percent-

age, the voltage is rapidly swept back to zero. Immediately after, a new sweep starts from zero voltage and the same process is repeated, thereby gradually narrowing the junction. The loop ends when the resistance measured at low bias is found to be above a certain predefined threshold.

Figure 5 shows a typical evolution of the feedback-controlled EB process. Normally, during the first voltage ramp (red trace in figure 5), non-linear I-V characteristics are observed, probably due to the removal of contaminants induced by current annealing (Nef, 2014; Moser, 2007). Increasing the voltage further, the first EB event is induced, as can be inferred from the downward curvature in the I-V characteristics. When the resistance increase triggers the feedback control, the voltage is set back to 0V and a new ramp is started. As the EB process evolves, the junction resistance increases by steps and the voltage at which the EB occurs decreases (as indicated by the green arrow in Figure 5).

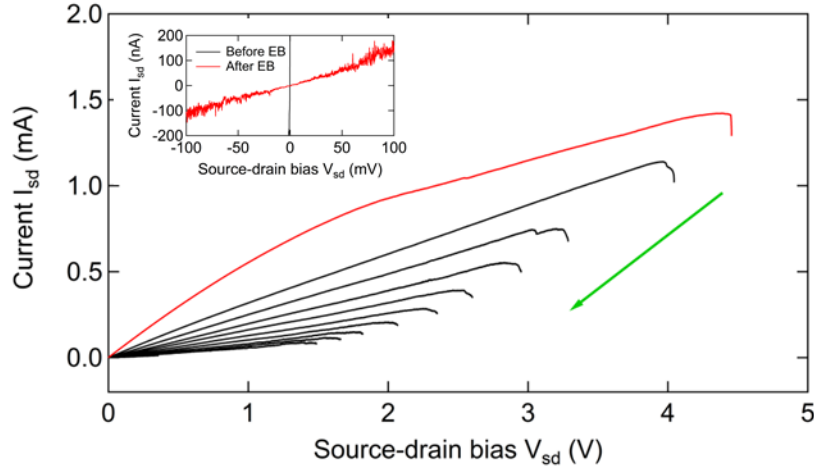


Figure 5. Sequence of I-V characteristics during a feedback-controlled EB process. A voltage ramp is applied between source and drain contacts until a drop in the current is observed (EB onset), corresponding to a resistance increase by more than a predefined percentage within the last 100 mV. The feedback loop stops the process to avoid the complete burning of the junction and starts a new ramp immediately after. The resistance increases at each step until a threshold value is attained. The inset shows the current in the junction after EB process.

With this EB process it is possible to obtain graphene based electrodes with nm-sized gaps displaying low-bias resistances in the range of $10^9 - 10^{10} \Omega$ at room temperature. However, most of the experimental measurements on molecular devices are carried out at ultra-low temperatures (see section 6). We have found that junctions with low-bias resistances higher than $\sim 10^6 \Omega$ at room temperature, typically, after the cooling, exhibit no tunneling current even up to high bias voltages of the order of 1V, which is usually considered the signature of the creation of a

large gap ($> 10\text{nm}$) not suitable for contacting one or few molecules. This effect is likely due to a mechanical contraction of the graphene electrodes when cooled down to cryogenic temperatures, which translates into an enlargement of the gap. To avoid this, we stop the EB process when the room temperature low-bias resistance is between $\sim 10^5$ and $\sim 10^6 \Omega$. At this point the I-V characteristics still have a finite linear slope (see inset of figure 5), suggesting that the gap formation is not yet complete. The final opening of the gap with size suitable to trap one or few molecules is achieved during the cooling.

In a first set of experiment, we have performed EB on 27 junctions of which 24 (89%) were controllably led to a low-bias resistance in the range of $100 \text{ k}\Omega$ to $3 \text{ M}\Omega$. In the other cases the feedback was not fast enough to respond, resulting in the formation of gaps with too high resistance ($> 1 \text{ G}\Omega$).

Figure 6 shows a SEM image of a typical graphene junction after EB, cool down to $\sim 100\text{mK}$ and subsequent return to room temperature: a few nanometer-wide gap is visible in the central region of the graphene constriction. The fact that the gap opening occurs in the patterned middle region is not surprising: the reduced cross section ensures that in that point the current density has the largest value, which favors the rupture of graphene.

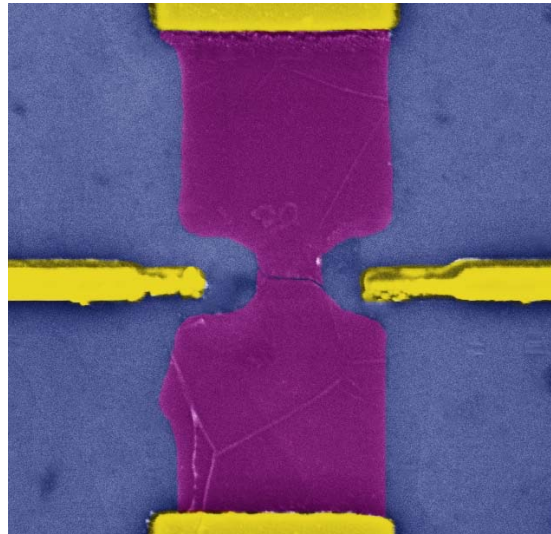


Figure 6. Nano-junction in graphene electrode (false colors): a gap in the junction is visible at SEM after the EB process.

4 Molecule with magnetic fingerprint.

TbPc₂ (figure 7a) is a prototypical case of single-ion magnetic molecule that has been largely used in several experiments thanks to its specific magnetic features and robustness when deposited on surfaces. Moreover, TbPc₂ perfectly suit to the single molecule transistor configuration as adding one electron to the read-out dot will not affect the charge state of the Tb ion, since this would require an oxidation or reduction of the terbium. Indeed, it was shown that up to the fifth reduction and second oxidation of the molecule, electrons are only added to the organic ligands (Zhu P., 2004). The magnetic center of this molecule is a Tb³⁺ ion which has a ground state with a total magnetic moment J=6 (S=3, L=3). In addition to the electronic spin, the Tb³⁺ ion carries a nuclear spin I = 3/2 with 100% abundance. The hyperfine interaction between the electron and the nuclear spin results in a fourfold splitting of each electronic level and introduces a dependence of the crossing point on the nuclear-spin state.

The Hamiltonian describing the TbPc₂ molecular nanomagnet can therefore be written as the sum of three contributions: interaction with the ligand field, hyperfine coupling and Zeeman effect (caused by the application of an external magnetic field).

The magnetic moment of the Tb ion is subjected to a ligand field mainly defined by the length of its covalent bonds and by the symmetry of the SMM. Inside the complex the Tb³⁺ ion is 8-fold coordinated to the nitrogen atoms of the two phthalocyanine ligands (see figure 7a). The Hamiltonian describing this ligand field interaction is given by (Ishikawa N. S., 2003):

$$\mathbf{H}_{LF} = A_2^0 \langle r^2 \rangle u_2 \mathbf{O}_2^0 + \langle r^4 \rangle u_4 (A_4^0 \mathbf{O}_4^0 + A_4^4 \mathbf{O}_4^4) + A_6^0 \langle r^6 \rangle u_6 \mathbf{O}_6^0$$

where the matrices \mathbf{O}_k^q are the Stevens operators (Abragam, 2012), $A_k^q \langle r^k \rangle$ the ligand field parameters (Ishikawa N. S., 2003; Ishikawa N. S., 2005) and u_k the constant coefficients introduced by Stevens (Stevens, 1952) and related to the ion ($u_2 = -1/99$, $u_4 = 2/16335$, $u_6 = -1/891891$). The terms \mathbf{O}_k^0 contain the operator J_z up to the k -th power and introduce a strong uniaxial anisotropy in the z direction.

When an external magnetic field \mathbf{B} is applied to the single-molecule magnet, the effect on the energy levels can be described by the Zeeman Hamiltonian:

$$\mathbf{H}_Z = g_J \mu_B \mathbf{J} \cdot \mathbf{B}$$

where $g_J = 1.5$ is the terbium's Landé g-factor and μ_B the Bohr magneton.

An exact numerical diagonalization of $\mathbf{H}_{LF} + \mathbf{H}_Z$ leads to the Zeeman diagram depicted in figure 7b (Ishikawa N. S., 2005). The ligand field induces an energy gap of 600 K between the ground state $|6, \pm 6\rangle$ and the first excited state $|6, \pm 5\rangle$. Hence, already at liquid nitrogen temperatures, the magnetic properties of this molecule are almost exclusively determined by the ground state doublet $m_J = \pm 6$:

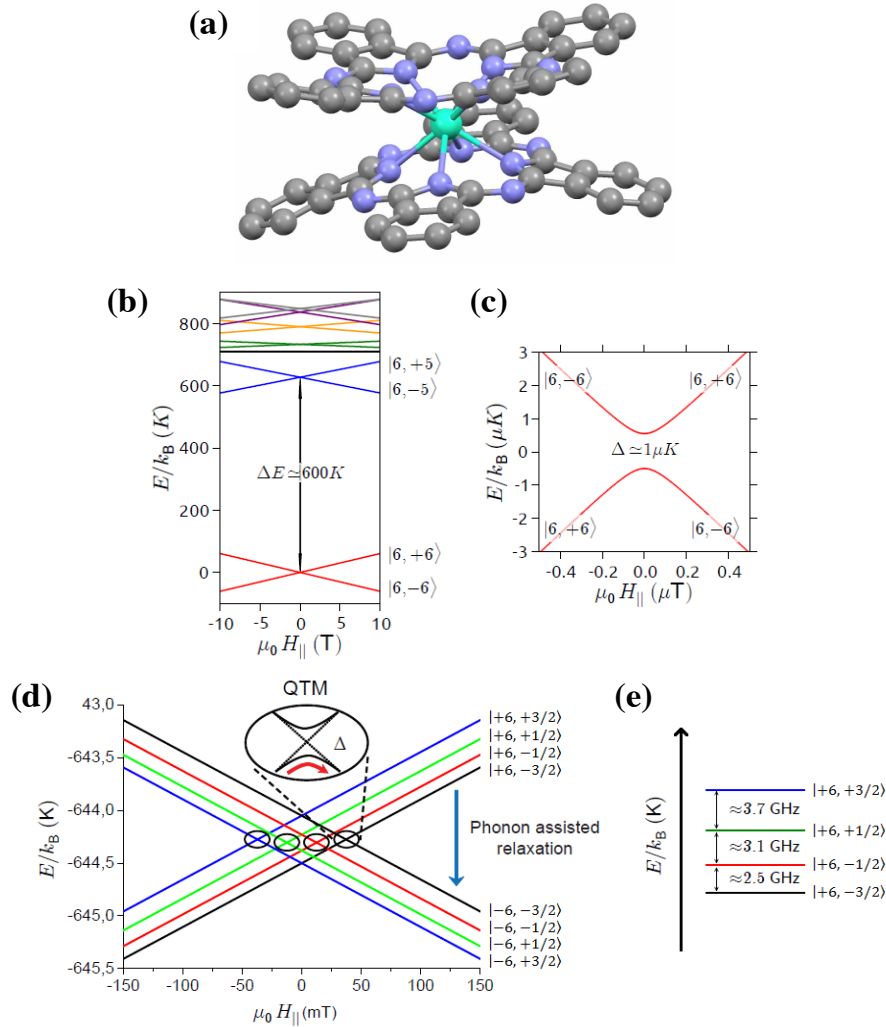


Figure 7. (a) Molecular TbPc₂ double decker: Tb (light green), N (light blue); C (gray). (b) Zeeman diagram of the TbPc₂. The ligand field splits the ground state (red) and first excited state (blue) by about 600 K, leaving only two spin degrees of freedom at low temperature, which makes the TbPc₂ SMM an Ising-like quantum system. (c) Zoom on the ground state doublet. Off-diagonal terms in the ligand field Hamiltonian lift the degeneracy of the ground state doublet by $\Delta \sim 1 \mu\text{K}$ and introduce an avoided level crossing in the Zeeman diagram. (d) Zeeman diagram presenting the energy of the two ground states $J_z = \pm 6$ as a function of the magnetic field. Due to the hyperfine coupling with the nuclear spin $I = 3/2$, each electronic ground state is split into four. Lines with the same color correspond to the same nuclear spin state (blue $|+3/2\rangle$, green $|+1/2\rangle$, red $| -1/2\rangle$, black $| -3/2\rangle$). The colored circles indicate avoided level crossing between two states of opposite electronic spin and identical nuclear spin. (e) Energy spacing between the different nuclear spin states for electronic magnetic moment $J_z = +6$ at small magnetic fields.

the TbPc₂ SMM can thus be seen as an Ising-like spin system at low temperatures. The highly anisotropic character of the Tb spin can thus be used as a fingerprint to recognize the actual presence of the molecule in the molecular transistor. Furthermore, the presence of the term $A_4^4 \langle r^4 \rangle u_4 \mathbf{O}_4^4$ in \mathbf{H}_{LF} is due to the fact that, because of π - π interactions between ligands, the two Pc planes are not exactly rotated by 45° (Koike, 1996). This term does not modify the general behavior of the Zeeman diagram, but it mixes the $m_j = +6$ and $m_j = -6$ in third order perturbation causing their degeneracy to be lifted by $\Delta \sim 1 \mu\text{K}$ (see figure 7c). This avoided level crossing gives rise to zero field quantum tunneling of the magnetization.

Finally, the hyperfine interaction (coupling the electronic spin \mathbf{J} with the nuclear spin \mathbf{I}) and the nuclear anisotropy (accounting for the quadrupole moment of the nuclear spin due to the non-perfectly spherical shape of the nucleus) need to be included. The resulting hyperfine Hamiltonian \mathbf{H}_{HF} is given by (Ishikawa N. S., 2005):

$$\mathbf{H}_{HF} = A\mathbf{I} \cdot \mathbf{J} + P \left[I_z^2 - \frac{1}{3}I(I+1) \right]$$

where $\mathbf{I} \cdot \mathbf{J} = I_z J_z + \frac{1}{2}(I_+ J_- + I_- J_+)$, A is the hyperfine coupling strength and P the quadrupole moment of the nucleus. MicroSQUID measurements performed on TbPc₂ molecular crystals have shown that $A = 24.9 \text{ mK}$ and $P = 14.4 \text{ mK}$ (Ishikawa N. S., 2005).

The numerical diagonalization of the full Hamiltonian $\mathbf{H} = \mathbf{H}_{LF} + \mathbf{H}_{HF} + \mathbf{H}_Z$ at different magnetic fields results in the Zeeman diagram reported in figure 7d, where the eight lowest lying eigenstates are represented. Due to the hyperfine interaction, each electronic ground state is split into four. The lines with a positive (negative) slope correspond to the electronic spin $|+6\rangle$ ($|-6\rangle$) and lines with the same color to the same nuclear spin state. The splitting of the electronic levels are unequal due to the quadrupole term of the hyperfine interaction, as depicted in figure 7e. Moreover, the anticrossing, which was formerly at $B = 0 \text{ T}$, is now split into four anticrossings, one for each nuclear spin state (see colored circles in figure 7d). The energy gap at each avoided level crossing remains about $1 \mu\text{K}$.

Changing the external magnetic field parallel to the easy axis of the TbPc₂ allows for the reversal of the molecule's magnetic moment. There exist two completely different reversal mechanisms: a direct relaxation (which dominates at larger magnetic fields) and the quantum tunneling of magnetization (QTM, which is predominant at smaller magnetic fields).

QTM is a tunnel transition between two different spin states $|S, m_s\rangle$ and $|S, m'_s\rangle$. It requires a finite overlap of the two wavefunctions, which is caused by the off-diagonal terms in the Hamiltonian (in the case of TbPc₂ this is due to the ligand field that gives rise to an avoided level crossing). When sweeping the magnetic field over these anticrossings, the spin can tunnel from the $|S, m_s\rangle$ into the

$|S, m'_s\rangle$ state with a probability P given by the Landau-Zener formula (Landau, 1932; Zener, 1932).

In addition to the QTM, the magnetic moment of the molecule can reverse in a direct transition. This is an inelastic process involving the creation and/or the annihilation of phonons to account for energy and momentum conservation (this is why it is referred to as phonon-assisted or spin-lattice relaxation). Three types of relaxation processes can be distinguished depending on the temperature. At low T the most likely spin reversal mechanism occurs through the emission of one phonon to the thermal bath (figure 8a). Increasing the temperature allows for a two-phonon relaxation process, in which the molecule is excited in a state $|e\rangle$ via the absorption of a phonon of energy $\hbar\omega_1$ and subsequently relaxes into the ground state through the emission of a phonon of energy $\hbar\omega_2$. This two-phonon relaxation mechanism is known as Orbach process (figure 8b) or Raman process (figure 8c) according to whether the excited state is real or virtual, respectively.

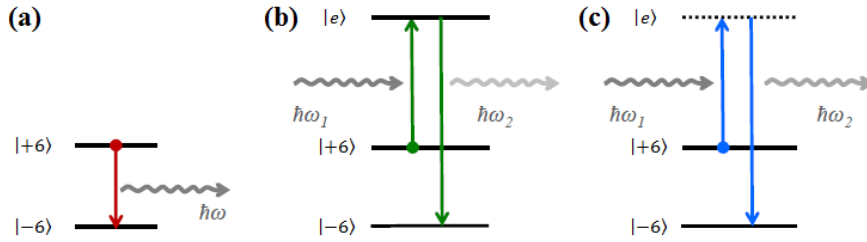


Figure 8. Spin-lattice relaxation processes. (a) Direct relaxation into the ground state involving the emission of a phonon with energy $\hbar\omega$. (b) Two-phonon Orbach process, in which the molecule is excited into the state $|e\rangle$ via the absorption of a phonon of energy $\hbar\omega_1$ and subsequently emits another phonon of energy $\hbar\omega_2$, thereby relaxing into its ground state. (c) Two-phonon Raman process, similar to the Orbach one but involving a virtual excited state. Hyperfine splitting of the ground state doublet was omitted for simplicity.

In order for a molecular magnet to be used in the framework of molecular spintronics, its magnetic properties need to be conserved when it is deposited on a conductive surface. XMCD (X-Ray Magnetic Circular Dichroism) measurements performed on isolated TbPc₂ molecules on different surfaces confirmed the robustness of the magnetic properties of single molecules with respect to the adsorption on a conductive substrate (Stepanow, 2010), (Candini A. e., 2016). In realistic situations, TbPc₂ molecules between electrodes can be affected by torsional deformations (Sorace, 2011), which slightly modify the term $A_4^4\langle r^4 \rangle$ in the ligand field Hamiltonian thus possibly slightly modifying the energy gap at avoided level crossing.

5 Realization of molecular devices.

To obtain our devices, we start by fabricating nano-gapped graphene electrodes, as described in detail in section 3. TbPc₂ micro-crystals are dissolved in dichloromethane and the solution is sonicated in order for the remaining TbPc₂ clusters to be completely dissolved. Graphene junctions are cleaned using acetone and isopropanol, then some droplets of the solution are deposited on the SiC chip and blow-dried with nitrogen. Recent studies have shown that TbPc₂ molecules are adsorbed on surface with the phthalocyanine planes parallel to the surface plane (Stepanow, 2010). Similar results have been reported for TbPc₂ on HOPG (Gopakumar, 2006) (Klar, 2014). However, due to the corrugation of the graphene surface and the presence of ripples (besides the local edge disorder introduced by electroburning), the orientation of the TbPc₂ molecule is expected to statistically present some misalignment leading to a finite tilt angle between the main device plane and the Pc plane (Candini A. K., 2011).

6. Low-temperature experiments

Molecular spin transistors are cooled down to ~ 80 mK in a dilution fridge equipped with a 3D vector magnet allowing for magnetic field sweep rates up to 50 mT/s. Electrical measurements are carried out using the lock-in technique with an AdWin-Pro system (16 bit output and 18 bits input) and a FEMTO pre-amplifier.

First, the low-temperature low-bias (1mV) differential conductance dI/dV is measured as a function of the gate voltage V_g . The device typically exhibits an insulating behavior for all the accessible gate regions, except for one or few Coulomb peaks (two examples are provided in figure 9).

To characterize the charge transport through the device, both the bias and the gate voltage are swept, allowing for the construction of a differential conductance map. Figure 10 provides some examples. The stability diagrams exhibit typical Coulomb diamond-like characteristics, confirming that charge transport through our devices is in the Coulomb blockade regime and can be modeled by one or few quantum dots in parallel. Interestingly, the conductance map on the left of figure 10 is characterized by the presence of several excited states that are clearly visible as multiple lines running parallel to the Coulomb diamond's edges.

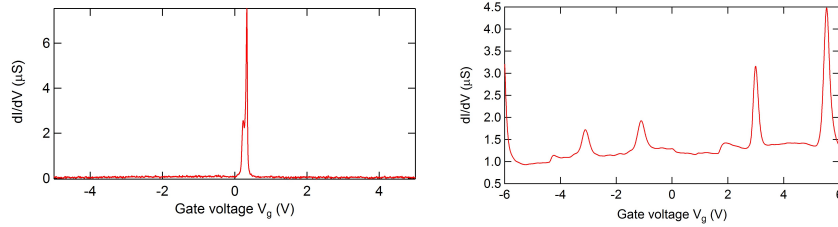


Figure 9. Differential conductivity dI/dV as a function of the applied gate voltage for two different junctions. Some Coulomb peaks are visible.

In a first set of experiments, after cooling, 5 out of 24 junctions (21%) exhibited Coulomb blockade-like features; 14 (58 %) either showed no dependence on the applied gate voltage (albeit being characterized by a measurable tunneling current for $|V_{ds}| < 0.5$ V) or were in short circuit with one of the corresponding lateral gates. Finally, 5 devices (21%) displayed no tunneling current for $|V_{ds}| < 1$ V (open gaps between the two electrodes).

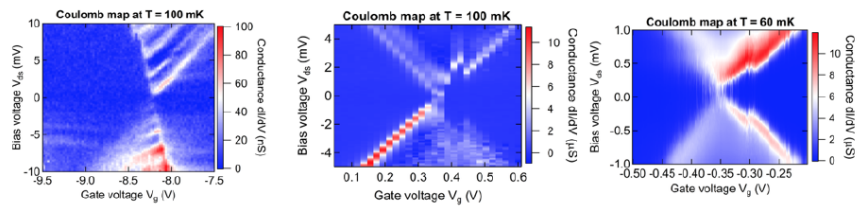


Figure 10. Color scale plots of the differential conductance dI/dV as a function of gate voltage V_g and source-drain bias V_{ds} resulting from measurements performed on three different samples. The appearance of the characteristic Coulomb diamonds indicates that the transport is in the Coulomb blockade regime. In the map on the left, several excited states are visible as lines running parallel to the diamond edges.

The spin properties of the $TbPc_2$ molecules are studied by the application of a magnetic field. Typically, only a small fraction of the tested devices (in our experiments $< 10\%$) show a reliable magnetic signal. Focusing only on one specific sample, the differential conductance $G(B)$ measured as a function of the magnetic field shows the opening of a hysteresis loop (figure 11), showing clear jumps in the conductivity vs the external field.

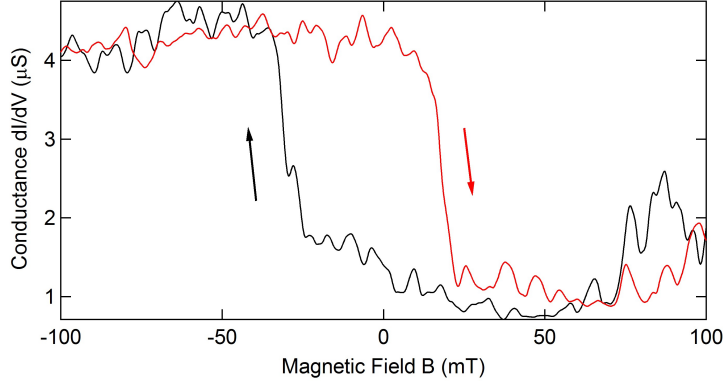


Figure 11. Zero-bias differential magnetoconductivity of a TbPc_2 molecular spin transistor obtained at constant gate voltage (V_g is fixed at a value close to a charge degeneracy point). The black curve corresponds to the magnetoconductivity under increasing field (trace) while for the red one the field is decreasing (retrace). The hysteresis is likely due to the magnetic moment reversal of the TbPc_2 SMMs deposited on the electroburnt graphene junctions.

The observed abrupt jumps in the conductance can be attributed to the switching of the TbPc_2 magnetic moment. As discussed in par.2, the Pc ligands in TbPc_2 molecule form a molecular quantum dot and the anisotropic magnetic moment of the Tb^{3+} ion is indirectly coupled to the electron path by an exchange interaction (Candini A. e., 2016). At low temperatures the Tb spin reversal induces a shift in the energy levels of Pc quantum dot that, in turns, provokes jumps in the conductivity by sweeping the magnetic field (see scheme Figure 2). The mechanism of this electronic read-out is therefore an indirect one: the current flows through one of the Pc ligands, which detects changes on the Tb electronic spin as a consequence of the exchange interaction.

The presence of the molecule between graphene electrodes is confirmed by the study of the angular dependence of the magnetic jumps as a function of the magnetic field orientation. In figure 12, the difference $\delta G(H)$ between the sweep up (trace) and down (retrace) of the magnetoconductance curves is plotted in color code for all the magnetic field directions in the (xy) plane of the device. The behavior reminds that of a magnetic system with uniaxial anisotropy and an easy axis of magnetization (indicated by a green arrow) can be identified. Upon a 45° tilt of the sample, the projection of the easy axis on the xy plane rotates by about 30° , suggesting that the field-sweep direction is not exactly aligned with the easy axis itself.

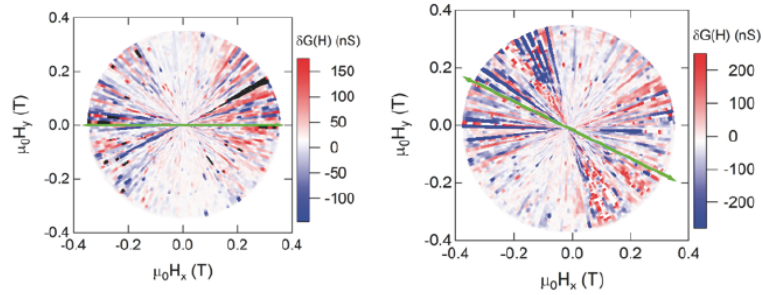


Figure 12. Color plot of the difference $\delta G(H)$ between trace and retrace for all directions of the magnetic field in the xy plane. The behavior is typical for magnetic systems exhibiting a uniaxial anisotropy. The easy axis is indicated by a green arrow and rotates by about 30° upon tilting the sample by 45° . Along the hard direction (perpendicular to the easy axis) no hysteresis is observed as the magnitude of the magnetic field is not high enough to reverse the magnetization of the system.

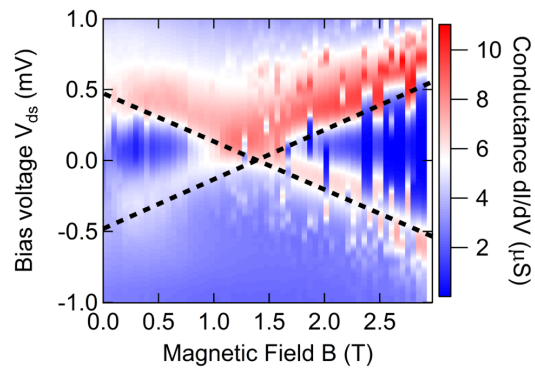


Figure 13. Differential conductance measured as a function of the source-drain voltage and the magnetic field at fixed gate voltage. An exchange coupling constant $a \sim 1,10$ T can be extracted.

As discussed in par.2, the origin of the magnetoconductance signal arises from the exchange coupling between the read-out quantum dot and the electronic spin of the Tb^{3+} metal ion (Thiele, 2014). The magnitude of the exchange coupling can be estimated by investigating the evolution of the splitting near a charge degeneracy point as a function of the applied magnetic field (figure 13). The splitting de-

creases linearly with increasing magnetic field and leads to a conductance peak at ~ 1.4 T which is the signature of the spin $\frac{1}{2}$ Kondo effect due to an odd number of electrons in the read-out quantum dot. The fact that the Kondo peak is split at zero magnetic field can be explained by a strong antiferromagnetic coupling to the terbium electronic spin. The magnitude of the coupling can be estimated via the formula (Vincent, 2012):

$$ag_J\mu_B J_z = k_B T_K + 2g\mu_B B_c$$

where g is the g -factor, μ_B the Bohr magneton, B_c the critical field (obtained extrapolating the Zeeman peaks at zero bias for positive values of the magnetic field), k_B the Boltzmann constant, T_K the Kondo temperature, $g_J\mu_B J_z$ the magnetic moment of the terbium and a a positive constant accounting for antiferromagnetic coupling. The Kondo temperature can be estimated from the half width at half maximum (HWHM) of the Kondo signature at $B_c = 1.4$ T using the approximate expression $HWHM = k_B T_K / e$ (Scott, 2010). Since $HWHM \sim 250$ μ V, a Kondo temperature $T_K \sim 2.9$ K can be inferred. By putting these values in the previous equation, a coupling constant $a \sim 1.10$ T can be derived. The efficient coupling between the two systems is probably due to the Pc unbound electron having $S = \frac{1}{2}$ which is close in energy to the Tb 4f state (Vitali, 2008).

Conclusions.

The way things work at molecular scale can be quite different from what we observe at the macroscopic scale due to the occurrence of both size and quantum effects. Thus, we need new concepts to design molecular devices. On top of this, we have to face extraordinary technological challenges to control matter and assemble devices at single molecular scale.

In this work we have presented our recent results on the realization and test of novel molecular spin transistors. To have these devices working, we have adopted specific solutions that now need to be further tested. The key idea for having functioning devices is to use a molecular quantum dot as ultra-sensitive detector to reveal the spin flip of a metal center tightly bound by exchange coupling. For this experiment we have used a very special molecule, the so called $[\text{TbPc}_2]^0$ single-ion magnet that, besides an extraordinary robustness, presents specific features such as the well-defined magnetic anisotropy of the Tb^{3+} ion and the presence of an unpaired electron delocalized over the two Pc ligands as $S = 1/2$ radical. This scheme allows, in principle, to preserve the valence of the magnetic center while charge current is passing in the molecular quantum dot. At the same time exchange coupling guarantees a sufficiently strong coupling between the spin center and its detector. It will be interesting to test how these features are essential for the design of new generations of molecular spin transistors.

For the realization of devices presented in this work we have used junctions obtained in graphene electrodes by electro-burning, instead of more conventional gold. Graphene presents flat carbon surface which may favor the contact with or-

ganic molecules and its chemical potential is expected to reduce the barrier with the molecular level, thus facilitating the electron conduction. Based on the results presented here, we believe that graphene can be considered as a suitable platform for contacting molecules and for the realization of complex electronic architectures at molecular scale.

Acknowledgements.

This work has been partially supported by European Community through the FET-Proactive Project “*MoQuaS*”, contract N.610449, and by the Italian Ministry for Research (MIUR) through the FIR grant RBFR13YKWX.

References

- (Sun, 2014) Sun, L., Diaz-Fernandez, Y. A., Gschneidner, T. A., Westerlund, F., Lara-Avila, S. and Moth-Poulsen, K., *Chem. Soc. Rev.* **43**, 7378-7411 (2014), doi:10.1039/c4cs00143e
- (Aviram, 1974) Aviram, A. and Ratner, M. A., *Chem. Phys. Lett.* **29**, 277 (1974), doi:10.1016/0009-2614(74)85031-1
- (Park H. P., 2000) Park, H., Park, J., Lim, A. K. L., Anderson, E. H., Alivisatos, A. P. and McEuen, P. L., *Nature* **407**, 57 (2000), doi:10.1038/35024031
- (Osorio, 2007) Osorio, E. A., O'Neill, K., Stuhr-Hansen, N., Nielsen, O. F., Bjørnholm, T. and van der Zant, H. S. J., *Adv. Mater.* **19** (2), 281 (2007), doi:10.1002/adma.200601876
- (Kubatkin, 2003) Kubatkin, S., Danilov, A., Hjort, M., Cornil, J., Bredas, N., Stuhr-Hansen, J. L., Hedegard, P. and Bjørnholm, T., *Nature* **425**, 698 (2003), doi:10.1038/nature02010
- (Park J. P., 2002) Park, J., Pasupathy, A. N., Goldsmith, J. I., Chang, C., Yaish, Y., Petta, J. R., Rinkoski, M., Sethna, J. P., Abruna, H. D., McEuen, P. L. and Ralph, D. C., *Nature* **417**, 722 (2002), doi:10.1038/nature00791
- (Liang, 2002) Liang, W. J., Shores, M. P., Bockrath, M., Long, J. R. and Park, H., *Nature* **417**, 725 (2002), doi:10.1038/nature00790
- (Lörtscher, 2013) Lörtscher, E., *Nature Nanotechnol.* **8**, 381–384 (2013), doi:10.1038/nnano.2013.105
- (Bumm, 1996) Bumm, L. A., Arnold, J. J., Cygan, M. T., Dunbar, T. D., Burgin, T. P., Jones, T. P., Allara, D. L., Tour J. M. and Weiss, P. S., *Science* **271**, 1705–1707 (1996), doi:10.1126/science.271.5256.1705
- (Reed, 1997) Reed, M. A., Zhou, C., Muller, C. J., Burgin, T. P. and Tour, J. M., *Science* **278**, 252–254 (1997), doi:10.1126/science.278.5336.252
- (Park H. L., 1999) Park, H., Lim, A. K. L., Alivisatos, A. P., Park, J. and McEuen, P. L., *Appl. Phys. Lett.* **75**, 301–303 (1999), doi:10.1063/1.124354
- (Moth-Poulsen, 2009) Moth-Poulsen, K. and Bjørnholm, T., *Nature Nanotechnol.* **4**, 551–556 (2009), doi:10.1038/nnano.2009.176
- (Ratner, 2013) Ratner, M., *Nature Nanotechnol.* **8**, 378–381 (2013), doi:10.1038/nnano.2013.110
- (Perrin, (2013)) Perrin, M. L., Verzijl, C. J. O., Martin, C. A., Shaikh, A. J., Eelkema, R., van Esch, J. H., van Ruitenbeek, J. M., Thijssen, J. M., van der Zant, H. S. J. and Dulić, D., *Nature Nanotechnol.* **8**, 282-287 (2013)
- (Bergvall, 2011) Bergvall, A., Berland, K., Hyldgaard, P., Kubatkin, S. and Löfwander, T., *Phys. Rev. B* **84**, 155451 (2011), doi:10.1103/PhysRevB.84.155451
- (García-Suárez, 2013) García-Suárez, V. M., Ferradás, R., Carrascal, D. and Ferrer, J., *Phys. Rev. B* **87**, 235425 (2013), doi:10.1103/PhysRevB.87.235425
- (Ryndyk, 2012) Ryndyk, D. A., Bundesmann, J., Liu, M.-H. and Richter, K., *Phys. Rev. B* **86**, 195425 (2012), doi:10.1103/PhysRevB.86.195425

- (Péterfalvi, 2012) Péterfalvi, C. G. and Lambert, C. J., *Phys. Rev. B* **86**, 085443 (2012), doi:10.1103/PhysRevB.86.085443
- (Prasongkit, 2013) Prasongkit, J., Grigoriev, A., Pathak, B., Ahuja, R. and Scheicher, R. H., *J. Phys. Chem. C* **117**, 15421–15428 (2013), doi:10.1021/jp4048743
- (Pshenichnyuk, 2013) Pshenichnyuk, I. A., Coto, P. B., Leitherer, S. and Thoss, M., *J. Phys. Chem. Lett.* **4**, 809–814 (2013), doi:10.1021/jz400025q
- (Prins F. B.-A., 2011) Prins, F., Barreiro, A., Ruitenberg, J. W., Seldenthuis, J. S., Aliaga-Alcalde, N., Vandersypen, L. M. K. and van der Zant, H. S. J., *Nano Lett.* **11**, 4607–4611 (2011), doi:10.1021/nl202065x
- (Cao Y. D., 2012) Cao, Y., Dong, S., Liu, S., He, L., Gan, L., Yu, X., Steigerwald, M. L., Wu, X., Liu, Z. and Guo, X., *Angew. Chem. Int. Ed.* **51**, 12228–12232 (2012), doi:10.1002/anie.201205607
- (Jia, 2013) Jia, C., Wang, J., Yao, C., Cao, Y., Zhong, Y., Liu, Z., Liu, Z. and Guo, X., *Angew. Chem. Int. Ed.* **52**, 1–6 (2013), doi:10.1002/anie.201304301
- (Cao Y. D., 2013) Cao, Y., Dong, S., Liu, S., Liu, Z. and Guo, X., *Angew. Chem. Int. Ed.* **52**, 3906–3910 (2013), doi:10.1002/anie.201208210
- (Burzurí E. P., 2012) Burzurí, E., Prins, F. and van der Zant, H. S. J., *Graphene* **01**, 26–29 (2012), doi:10.4236/graphene.2012.12004
- (Nef, 2014) Nef, C., Pósa, L., Makk, P., Fu, W., Halbritter, A., Schönenberger, C. and Michel, C., *Nanoscale* **6**, 7249–7254 (2014), doi:10.1039/c4nr01838a
- (Lau, 2014) Lau, C. S., Mol, J. A., Warner, J. H. and Briggs, G. A. D., *Phys. Chem. Chem. Phys.* **16**, 20398–20401 (2014), doi:10.1039/c4cp03257h
- (Kim, 2009) Kim, K. S., Zhao, Y., Jang, H., Lee, S. Y., Kim, J. M., Kim, K. S., Ahn, J.-H., Kim, P., Choi, J.-Y. and Hee, B., *Nature* **457**, 706 (2009), doi:10.1038/nature07719
- (Zyasin, 2010) Zyasin, A. S., van den Berg, J. W. G., Osorio, E. A., van der Zant, H. S. J., Konstantinidis, N. P., Leijnse, M., Wegewijs, M. R., May, F., Hofstetter, W., Danieli C. and Cornia A., *Nano Lett.* **10**, 3307 (2010), doi:10.1021/nl1009603
- (Vincent, 2012) Vincent, R., Klyatskaya, S., Ruben, M., Wernsdorfer, W. and Balestro, F., *Nature* **488**, 357 (2012), doi:10.1038/nature11341
- (Burzurí E. Z., 2012) Burzurí, E., Zyasin, A. S., Cornia, A. and van der Zant, H. S. J., *Phys. Rev. Lett.* **109**, 147203 (2012), doi:10.1103/PhysRevLett.109.147203
- (Bogani, 2008) Bogani, L. and Wernsdorfer, W., *Nature Materials* **7**, 179–186 (2008), doi:10.1038/nmat2133
- (Thiele, 2014) Thiele, S., Balestro, F., Ballou, R., Klyatskaya, S., Ruben, M. and Wernsdorfer W., *Science* **344**, 1135–1138 (2014), doi:10.1126/science.1249802
- (Forbeaux, 1998) Forbeaux, I., Themlin, J. M. and Debever, J. M., *Phys. Rev. B* **58**, 16396–16406 (1998), doi:10.1103/PhysRevB.58.16396
- (Berger, 2004) Berger, C., Song, Z., Li, T., Li, X., Ogbazghi, A. Y., Feng, R., Dai, Z., Marchenkov, A. N., Conrad, E. H., First, P. N. and de Heer, W. A., *J. Phys. Chem. B* **108**, 19912–19916 (2004), doi:10.1021/jp040650f

- (Ohta, 2006) Ohta, T., Bostwick, A., Seyller, T., Horn, K. and Rotenberg, E., *Science* **313**, 951–954 (2006), doi: 10.1126/science.1130681
- (Virojanadara, 2008) Virojanadara, C., Syväjärvi, M., Yakimova, R., Johansson, L. I., Zakharov, A. A. and Balasubramanian, T., *Phys. Rev. B*, **78**, 245403 (2008), doi:10.1103/PhysRevB.78.245403
- (Hanson, 2007) Hanson, R., Kouwenhoven, L. P., Petta, J. R., Tarucha, S. and Vandersypen, L. M. K., *Rev. Mod. Phys.* **79**, 1217-1265 (2007), doi:10.1103/RevModPhys.79.1217
- (Candini A. e., 2016) Candini, A., Klar, D., Marocchi, S., Corradini, V., Biagi, R., De Renzi, V., del Pennino, U., Troiani, F., Bellini, V., Klyatskaya, S., Ruben, M., Kummer, K., Brookes, N. B., Huang, H., Soncini, A., Wende, H. and Affronte, M., *Sci. Rep.* **6**, 21740 (2016)
- (Frewin, 2009) Frewin, C. L., Coletti C., Riedl, C., Strake, U., Sadow, S. E., *Mater. Sci. Forum* **615-617**, 589-592 (2009), doi:10.4028/www.scientific.net/MSF.615-617.589
- (Starke, 2012) Starke, U., Forti, S., Emtsev, K. V. and Coletti, C., *MRS Bull.* **37**, 1177–1186 (2012), doi:10.1557/mrs.2012.272
- (Shivaraman, 2009) Shivaraman, S., Chandrashekhar, M. V. S., Boeckl, J. J., Spencer, M. G. J., *Electron. Mater.* **38**, 725–730 (2009), doi:10.1007/s11664-009-0803-6
- (Candini A. R., 2015) Candini, A., Richter, N., Convertino, D., Coletti, C., Balestro, F., Wernsdorfer, W., Kläui, M. and Affronte, M., *Beilstein J. Nanotechnol.*, **6**, 711-719 (2015), doi:10.3762/bjnano.6.72
- (Prins F. H., 2009) Prins, F., Hayashi, T., van Steenwijk, B. J. A. D., Gao, B., Osorio, E. A., Muraki, K. and van der Zant, H. S. J., *Appl. Phys. Lett.* **94**, 123108 (2009), doi:10.1063/1.3109784
- (Moser, 2007) Moser, J., Barreiro, A. and Bachtold A., *Appl. Phys. Lett.* **91**, 163513 (2007), doi:10.1063/1.2789673
- (Zhu, 2004) Zhu, P., Lu, F., Pan, N., Arnold, D. P., Zhang, S. and Jiang, J., *Eur. J. Inorg. Chem.* **2004**, 510-517 (2004), doi:10.1002/ejic.200300509
- (Ishikawa N. S., 2003) Ishikawa, N., Sugita, M., Okubo, T., Tanaka, N., Iino, T. and Kaizu, Y., *Inorg. Chem.* **42**, 2440-2446 (2003), doi:10.1021/ic026295u
- (Abragam, 2012) Abragam, A. and Bleaney, B., *Electron Paramagnetic Resonance of Transition Ions (Oxford Classic Texts in the Physical Sciences)* (Oxford Univ. Press, New York, 2012), ISBN 978-0-19-965152-8
- (Ishikawa N. S., 2005) Ishikawa, N., Sugita, M. and Wernsdorfer, W., *Angew. Chem. Int. Ed.* **44**(19), 2931-2935 (2005), doi:10.1002/anie.200462638
- (Stevens, 1952) Stevens, K. W. H., *Proc. Phys. Soc. A* **65**, 209-215 (1952), doi:10.1088/0370-1298/65/3/308
- (Koike, 1996) Koike, N., Uekusa, H., Ohashi, Y., Harnooode, C., Kitamura, F., Ohsaka, T. and Tokuda, K., *Inorg. Chem.* **35**(20), 5798-5804 (1996), doi:10.1021/ic960158d
- (Landau, 1932) Landau, L. D., *Physics of the Soviet Union* **2**, 46-51 (1932)
- (Zener, 1932) Zener, C., *Proc. R. Soc. Lond. A* **137**, 696-702 (1932), doi:10.1098/rspa.1932.0165

- (Stepanow, 2010) Stepanow, S., Honolka, J., Gambardella, P., Vitali, L., Abdurakhmanova, N., Tseng, T.-C., Rauschenbach, S., Tait, S. L., Sessi, V., Klyatskaya, S., Ruben, M. and Kern, K., *J. Am. Chem. Soc.* **132**(34), 11900-11901 (2010), doi:10.1021/ja105124r
- (Sorace, 2011) Sorace, L., Benelli, C. and Gatteschi, D., *Chem. Soc. Rev.* **40**, 3092-3104 (2011), doi:10.1039/C0CS00185F
- (Gopakumar, 2006) Gopakumar, T. G., Muller, F. and Hietschold, M., *J. Phys. Chem. B* **110**, 6051-6065 (2006), doi:10.1021/jp060936f
- (Klar, 2014) Klar, D., Candini, A., Joly, L., Klyatskaya, S., Krumme, B., Ohresser, P., Kappler, J.-P., Ruben, M. and Wende, H., *Dalton Trans.* **43**, 10686-10689 (2014)
- (Candini A. K., 2011) Candini, A., Klyatskaya, S., Ruben, M., Wernsdorfer, W. and Affronte, M., *Nano Lett.* **11**, 2634-2639 (2011), doi:10.1021/nl2006142
- (Scott, 2010) Scott, D. G. and Natelson, D., *ACS Nano* **4**(7), 3560-3579 (2010), doi:10.1021/nn100793s
- (Vitali, 2008) Vitali, L., Fabris, S., Conte, A. M., Brink, S., Ruben, M., Baroni, S. and Kern, K., *Nano Lett.* **8**, 3364-3368 (2008), doi:10.1021/nl801869b